ACS APPLIED MATERIALS & INTERFACES

Research Article

www.acsami.org

ZnO/CoO and $ZnCo_2O_4$ Hierarchical Bipyramid Nanoframes: Morphology Control, Formation Mechanism, and Their Lithium Storage Properties

Jing Bai,[†] Kaiqi Wang,[†] Jinkui Feng,[†] and Shenglin Xiong*[,†,‡]

[†]Key Laboratory for Colloid and Interface Chemistry, Ministry of Education, and School of Chemistry and Chemical Engineering, Shandong University, Jinan 250100, P. R. China

[‡]Institute of Physical Chemistry, Zhejiang Normal University, Jinhua 321004, China

Supporting Information

ABSTRACT: Mastery over the structure of nanoscale materials can effectively tailor and regulate their electrochemical properties, enabling improvement in both rate capability and cycling stability. We report the shape-controlled synthesis of novel mesoporous bicomponent-active ZnO/CoO hierarchical multilayered bipyramid nanoframes (HMBNFs). The as-synthesized micro/nanocrystals look like multilayered bipyramids and consist of a series of structural units with similar frames and uniform sheet branches. The use of an appropriate straight-chain monoalcohol was observed to be critical for the formation of HMBNFs. In addition, the structure of HMBNFs could be preserved only in a limited range of the precursor ratio. An extremely fast crystal growth process and an unusual transverse crystallization of the ZnCo-carbonate HMBNFs were newly discovered and proposed. By calcination of ZnCo-carbonate HMBNFs at the atmosphere of nitrogen and air, ZnO/CoO and $ZnCo_2O_4$ HMBNFs were obtained, respectively. Compared to the $ZnCo_2O_4$ HMBNFs, the ZnO/CoO HMBNFs with a uniform distribution of nanocrystal ZnO and CoO subunits exhibited enhanced electrochemical activity, including greater rate capability and longer cycling performance, when evaluated as an anode material for Li-ion batteries. The superior electrochemical performance of the ZnO/CoO HMBNFs is attributed to the unique nanostructure, bicomponent active synergy, and uniform distribution of ZnO and CoO phases at the nanoscale.

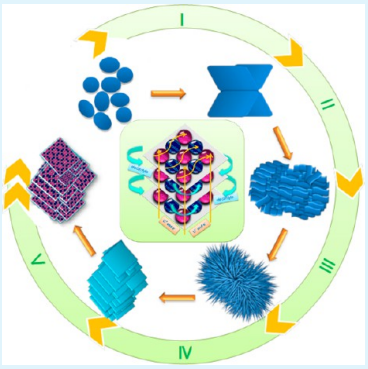

KEYWORDS: *bipyramid, nanoframes, synergistic effect, lithium-ion batteries, anodes*

1. INTRODUCTION

As a family of important power carriers, rechargeable Li-ion batteries (LIBs) have exhibited indispensability in various aspects of everyday life, including mobile devices, renewable energy storage, electric vehicles, and smart grids.[1−3] To satisfy the ever-growing demands of these applications, further improvements in energy density, rate capability, and cycle life are definitely required.[4−7] A commercial carbon-based anode is currently used in LIBs; however, other new candidate anode materials have been explored because the theoretical capacity of the carbon-based anodes is only 372 mA h g^{-1}. Among these candidates, transition metal oxides (TMOs) with higher specific capacities, such as CoO, Co_3O_4, MnO_2, and Fe_2O_3, are considered promising anode materials.[8−11] Nevertheless, the great volume change during lithiation and delithiation process results in the pulverization and agglomeration of electrodes, resulting in fast capacity fading, poor rate capability and low cycle stability.[2,8] Recently, many improvements have been demonstrated by finely tailoring these TMOs to composite materials. One common method is to integrate TMOs with graphene or carbon matrices; examples of such materials include MoO_2/grapheme,[12] CoO/grapheme,[13] Fe_3O_4/C,[14] SnOx/C,[15] FeOx@C,[16] and CoO/C,[8,17] which have been studied widely. The main advantage is that the improved conductivity of electrode materials, to some extent, can afford better lithium-ion storage behaviors. Another approach is to combine different types of TMOs, which opens up the possibility of achieving a higher capacity through the interaction of electroactive materials involved. Driven by their attractive advantages, numerous researchers have explored hybridized materials. Multistep routes are commonly used to fabricate hybrid materials, wherein the second material forms with the first material as the matrix. However, the resultant hybrid materials are characterized by a random and uneven distribution of components. Thus far, few documents have reported the endeavors of composites with a homogeneous dispersion of constituents, such as CoO/$CoFe_2O_4$,[18] ZnO/$ZnFe_2O_4$,[19] and Co_3O_4/$CoFe_2O_4$.[20] Hence, enhancing the properties of these hybrid materials as LIB electrode materials that exhibit both long cycle stability as well as high capacity retention remains a significant challenge.

Received: June 15, 2015
Accepted: October 2, 2015
Published: October 2, 2015

ACS Publications © 2015 American Chemical Society

DOI: 10.1021/acsami.5b05303
ACS Appl. Mater. Interfaces 2015, 7, 22848−22857

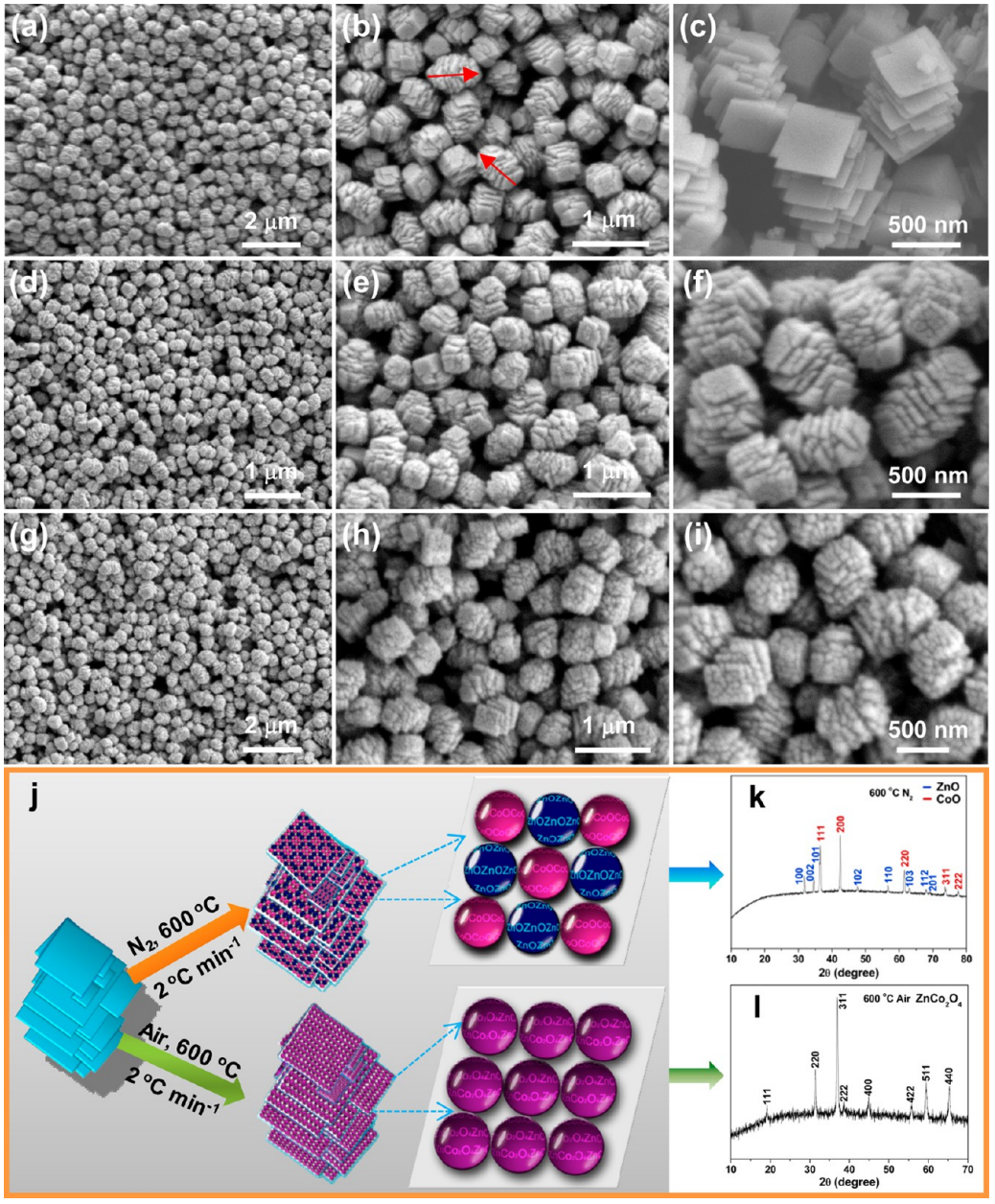

Figure 1. Morphological and structureal characterization: (a–c) FESEM images of $Zn_{0.33}Co_{0.67}CO_3$ HMBNFs; (d–f) ZnO/CoO HMBNFs; (g–i) $ZnCo_2O_4$ 3D HMBNFs; (j) schematic of the process of preparing ZnO/CoO HMBNFs and $ZnCo_2O_4$ HMBNFs; (k) XRD patterns of ZnO/CoO HMBNFs; and (l) XRD patterns of $ZnCo_2O_4$ HMBNFs.

Assembled TMOs have attracted ever-increasing attention, especially the 3D porous hierarchical structures consisting of nanosized subunits. These materials offer prominent superiority when used as LIB anodes. First, nanostructured materials not only can provide high contact area for active materials and electrolytes but also shorten the Li^+ diffusion path. Second, the features of porous structures can relieve the pulverization and agglomeration caused by the volume change, helping the electrode maximize contact with the electrolyte and offering a buffer for volume expansion and contraction. Furthermore, the structural voids constructed by nanometer-size particles can promote the penetration of electrolyte and the intercalation of Li^+ by providing numerous suitable porous channels. Because of their combination of the aforementioned notable features, porous nanocomposite architectures are an ideal electrode candidate. In particular, the structure configuration of homogeneously integrated TMO nanocomposites provides an effective approach to enhancing the electrochemical performance. Notably, the nanocomposites (NCs) that have been previously reported are usually a combination of binary and ternary TMOs (biter-NCs); the literature contains few studies involving the hybridization of two binary TMOs (bibi-NCs).[18−20] Moreover, a stable and long cycling performance with high reversible capacity has not been satisfactorily achieved in the previous works.[18−20] 3D hybrid porous hierarchical microstructures fulfill the practical requirements as well as represent a fascinating and significant potential. Therefore, further investigations are needed to develop more efficient assembly motifs of bibi-NCs to obtain materials with excellent electrochemical performance.

Herein, we have prepared a novel, well-designed bibi-NC system-micro/nanostructured ZnO/CoO hierarchical nano-

DOI: 10.1021/acsami.5b05303
ACS Appl. Mater. Interfaces 2015, 7, 22848−22857

hybrids-via calcination of a ZnCo-carbonate precursor prefabricated by a facile solution-based method under an N_2 atmosphere. As far as we know, this work represents the first report of the fabrication of mesoporous ZnO/CoO hierarchical multilayered bipyramid nanoframes (HMBNFs). The obtained bipyramid-shaped micro/nanocrystals are composed of a series of similar sheet branches. When the precursor is annealed in air, $ZnCo_2O_4$ HMBNFs can be instead attained. Variation of the amount of NH_4HCO_3 involved in the system could optimize the preparation of HMBNFs. The structure of alcohol was observed to be critical to the formation of HMBNFs. Furthermore, the morphological evolution of the corresponding precursor was investigated in detail. More interesting is that an unusual fast-growth mechanism and an extraordinary morphology change during the crystallization process were observed for the first time. In general, when ZnO and CoO have been used independently as LIBs, their drastic volume change during lithiation and delithiation process and poor inherent electronic conductivity lead to poor cycling stability and rate capability. However, when tested as anodes for LIBs in this work, both ZnO/CoO and $ZnCo_2O_4$ HMBNFs exhibited superior electrochemical performance. More surprisingly, ZnO/CoO exhibited better performance, with superior cycle stability and greater reversible capacity compared to $ZnCo_2O_4$. The excellent electrochemical activity of ZnO/CoO is attributed to the unique configuration of HMBNFs and synergetic effects of the different components demonstrated by lots of reports.

2. MATERIALS AND METHODS

2.1. Synthesis of ZnO/CoO Hierarchical Multilayered Bipyramid Nanoframes (HMBNFs). The detailed synthesis process of ZnO/CoO HMBNFs was described as follows: 0.22 g of $Zn(CH_3COO)_2 \cdot 2H_2O$ (1 mmol), 0.5 g of $Co(CH_3COO)_2 \cdot 4H_2O$ (2 mmol) and 1.2 g of NH_4HCO_3 (15 mmol) were dissolved in 50 mL of n-pentanol under magnetic stirring. After 40 min of stirring, the transparent mixture solution was transferred into a 75 mL Teflon-lined autoclave and maintained at 200 °C for 20 h. The product was deep pink precipitates and centrifuged with deionized water and absolute ethanol several times. Finally, the deep pink powders was obtained as the precursor after drying at 60 °C for 12h. The green powder (ZnO/CoO) and the black powder ($ZnCo_2O_4$) were obtained by annealing the precursor at 600 °C for 6 h in nitrogen and air, respectively.

2.2. Characterization of Materials. The products were characterized by X-ray diffraction powder (XRD, Philips X'Pert Pro Super diffractometer, Cu Kα radiation, λ = 1.54178 Å). The morphology, dimension and chemical composition of the samples were analyzed using transmission electron microscopy (TEM, JEOL JEM 1011), field emission scanning electron microscopy (FESEM, JEOL JSM-6700F), and high-resolution transmission electron microscopy (HRTEM/EDX, JEM-2100F, 200 kV). Thermogravimetric analysis (TGA, PerkinElmer Diamond TG/DTA apparatus) was performed at a heating rate of 10 °C min^{-1} in flowing air and N_2, respectively. The texture properties of the products were measured by N_2 adsorption−desorption isotherms (Micromeritics Automatic Surface Area Analyzer Gemini 2360, Shimadzu) at 77 K. The surface feature and pore size distribution of the products were tested by Brunauer−Emmett−Teller (BET) method. The chemical states of the products were studied by X-ray photoelectron spectroscopy (XPS, VGESCA-LABMK II spectrometer, with a twin-anode Al Ka (1486.6 eV) X-ray source. All the binding energies were calibrated using C 1s peak (284.6 eV) as a reference.

2.3. Electrochemical Characterization. The electrochemical measurements were performed via 2032 coin-type cells assembled in an argon-filled glovebox with the concentrations of H_2O and O_2 below 0.2 ppm. To obtain the working electrodes, the samples, conductive material (acetylene black) and binder (carboxymethylcellulose sodium, NaCMC) were mixed in a weight ratio of 70:20:10. The black green slurry was pasted on the pure copper foil and dried at 80 °C in vacuum. The mass loading, the diameter, and the thickness of the working electrode materials is about 1 mg cm^{-2}, 12 mm, and 200 μm, respectively. Lithium metal foil of 14 mm in diameter was used as both the counter electrode and the reference electrode. The electrolyte was a mixture containing 1 M $LiPF_6$ in ethylene carbonate, dimethyl carbonate, diethyl carbonate in a volume ration of 1:1:1 purchased from Samsung Chemical Corporation. The galvanostatic charge/discharge measurements tested by CT2001A LAND Cell test system. The electrochemical performance was carried out at various current densities in the voltage range of 0.01−3.00 V.

3. RESULTS AND DISCUSSION

As shown in Figure 1a, b, the field-emission scanning electron microscopy (FESEM) images reveal the high yield of uniform $Zn_{0.33}Co_{0.67}CO_3$ HMBNFs with an average length of ~1 μm (denoted as the length along the aligning direction of the bipyramids, marked by arrows in Figure 1b). As evident in the higher-magnification image in Figure 1c, the HMBNFs are stacked by 2D nanosheets in a certain order; the corresponding X-ray diffraction (XRD) pattern is provided in the Figure S1. According to the thermogravimetric analysis (TGA) results (Figures S2 and S3), after the HMBNFs were annealed under N_2 at 600 °C, the multilayered nanohybrid ZnO/CoO HMBNFs were achieved, whereas the multilayered $ZnCo_2O_4$ HMBNFs were obtained after the HMBNFs were annealed under air at 600 °C. Despite thermal decomposition, both ZnO/CoO and $ZnCo_2O_4$ well-maintained the parental morphology of $Zn_{0.33}Co_{0.67}CO_3$ HMBNFs without structural collapse, as indicated by the FESEM images in Figure 1d−-f and Figure 1g−i, respectively. The HMBNFs are also highly uniform, with a size distribution similar to that of the $Zn_{0.33}Co_{0.67}CO_3$ precursor. The surfaces of these crystals become much rougher, and clear grain boundaries are obvious to be observed, suggesting the generation of a porous structure. The high-magnification FESEM images shown in Figure 1f, i further detail the resembling porous architecture, which is assembled by numerous smaller nanosized subclass building blocks in both samples.

As illustrated in Figure 1j, under different heat-treatment conditions, the precursor was transformed into two different products, namely multilayered hybrid ZnO/CoO and $ZnCo_2O_4$ HMBNFs. The diffraction peaks of (100), (002), (101), (102), (110), (103), (112), and (201) in Figure 1k are indexed as hexagonal ZnO (JCPDS card No. 36−1451). The remaining diffraction peaks of (111), (200), (220), (311), and (222) are defined as well-crystallized hexagonal CoO (JCPDS card No. 48−1719). No peaks due to impurities are present here, indicating that layered ZnO/CoO HMBNFs consist of only crystalline ZnO and CoO. All the diffraction peaks in the XRD pattern in Figure 1i are assigned exclusively to cubic spinel $ZnCo_2O_4$ (JCPDS Card No. 23−1390) with good crystallinity; no peaks are attributable to impurities. In this spinel structure, Zn^{2+} occupy the tetrahedral sites and Co^{3+} occupy the octahedral sites.[21] Further characterization of surface information and element valence with X-ray-photoelectron-spectroscopy (XPS) in the Figure S4. On the basis of the analysis results of XRD and XPS, ZnO/CoO and $ZnCo_2O_4$ are confirmed as the products obtained under N_2 and air atmospheres, respectively. The specific surface area and porosity of the hybrid ZnO/CoO and $ZnCo_2O_4$ were investigated by nitrogen adsorption/desorption at 77 K (Figure S5). The observed hysteresis feature is a typical type-IV isotherm with an H2-type loop, reflecting the mesoporous nature of the ZnO/CoO and

DOI: 10.1021/acsami.5b05303
ACS Appl. Mater. Interfaces 2015, 7, 22848−22857

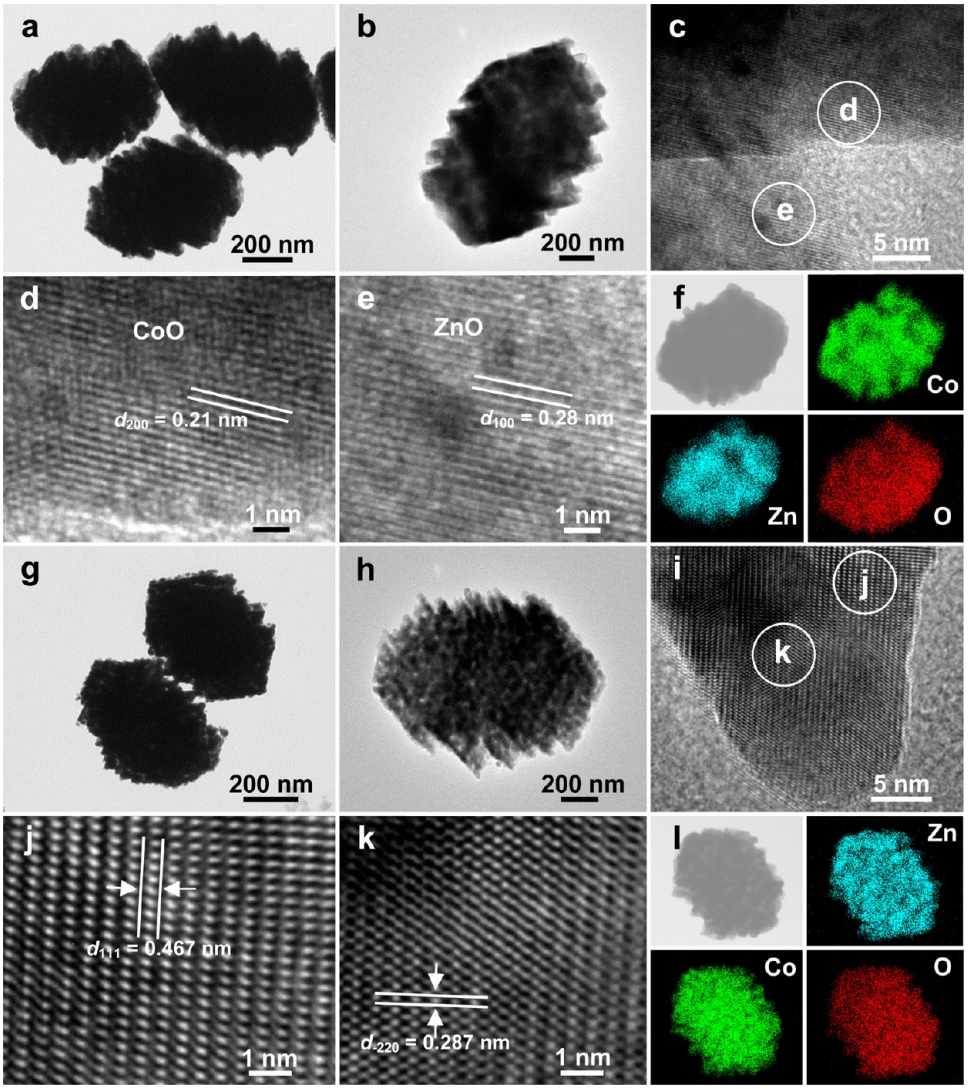

Figure 2. (a–e) TEM and HRTEM images of ZnO/CoO HMBNFs; (f) STEM image of ZnO/CoO HMBNFs and the corresponding elemental mapping images of Zn, Co, and O. (g–k) TEM and HRTEM images of $ZnCo_2O_4$ HMBNFs; (l) STEM image of $ZnCo_2O_4$ HMBNFs and the corresponding elemental mapping images of Zn, Co, and O.

$ZnCo_2O_4$ crystals. The pore size distribution curves are shown as the inset in Figure S5. Both ZnO/CoO and $ZnCo_2O_4$ HMBNFs exhibit a monomodal pore distribution, with mean pore sizes of 14.9 and 22.5 nm, respectively, and with pore sizes that range from 4 to 48 nm and from 4 to 46 nm, respectively. A small number of macropores in the range between 46 and 150 nm is also detectable in the $ZnCo_2O_4$ HMBNFs, which results from interparticle spaces. The specific BET surface areas of ZnO/CoO and $ZnCo_2O_4$ were determined to be 23.2 and 16.7 $m^2\ g^{-1}$, respectively.

The TEM images of several layered ZnO/CoO HMBNFs in Figure 2a, b are consistent with the aforementioned FESEM images that indicated the layered structure comprises many nanosized subunits. High-resolution TEM (HRTEM) images (Figure 2c–e) further prove that both ZnO and CoO exhibit fine crystallization in the ZnO/CoO HMBNFs. The two lattice fringes in the HRTEM images (Figure 2d, e), with fringe distances of 0.21 and 0.28 nm, correspond to *d*-spacings of $(200)_{CoO}$ and $(100)_{ZnO}$, respectively, which further confirms the coexistence of CoO and ZnO. The TEM and HRTEM images of $ZnCo_2O_4$ HMBNFs are also provided in Figure 2g–k, which clearly display that the layered structure is assembled by numerous nanosized subunits. The 0.467 and 0.287 nm values can be assigned to the (111) and (−220) interplane spacings of $ZnCo_2O_4$, respectively. To investigate the elemental distribution of Zn, Co, and O, we carried the ZnO/CoO HMBNFs out by scanning transmission electron microscopy (STEM). As illustrated in Figure 2f, the obtained mapping panels reveal that Zn, Co and O have a high quality of homogeneous distribution in the ZnO/CoO hybrids. Furthermore, the Zn/Co atomic ratio measured from the energy-dispersive X-ray spectroscopy (EDX) spectrum is 1.04:2 (Figure S6), which is consistent with the stoichiometric ratio of 1:2 for the phase-pure $Zn_{0.33}Co_{0.67}CO_3$ precursor. The detailed STEM investigation of $ZnCo_2O_4$ is presented in Figure 2l. EDX analysis confirms the formation of $ZnCo_2O_4$ with Zn, Co, and O as the principal elemental components and a Zn/Co molar ratio of 1.01:2 (Figure S7), which is in accord with the stoichiometric $ZnCo_2O_4$. The STEM and EDX elemental maps clearly indicated a uniform spatial distribution of Zn, Co, and O in the ZnO/CoO and $ZnCo_2O_4$ HMBNFs.

DOI: 10.1021/acsami.5b05303
ACS Appl. Mater. Interfaces 2015, 7, 22848–22857

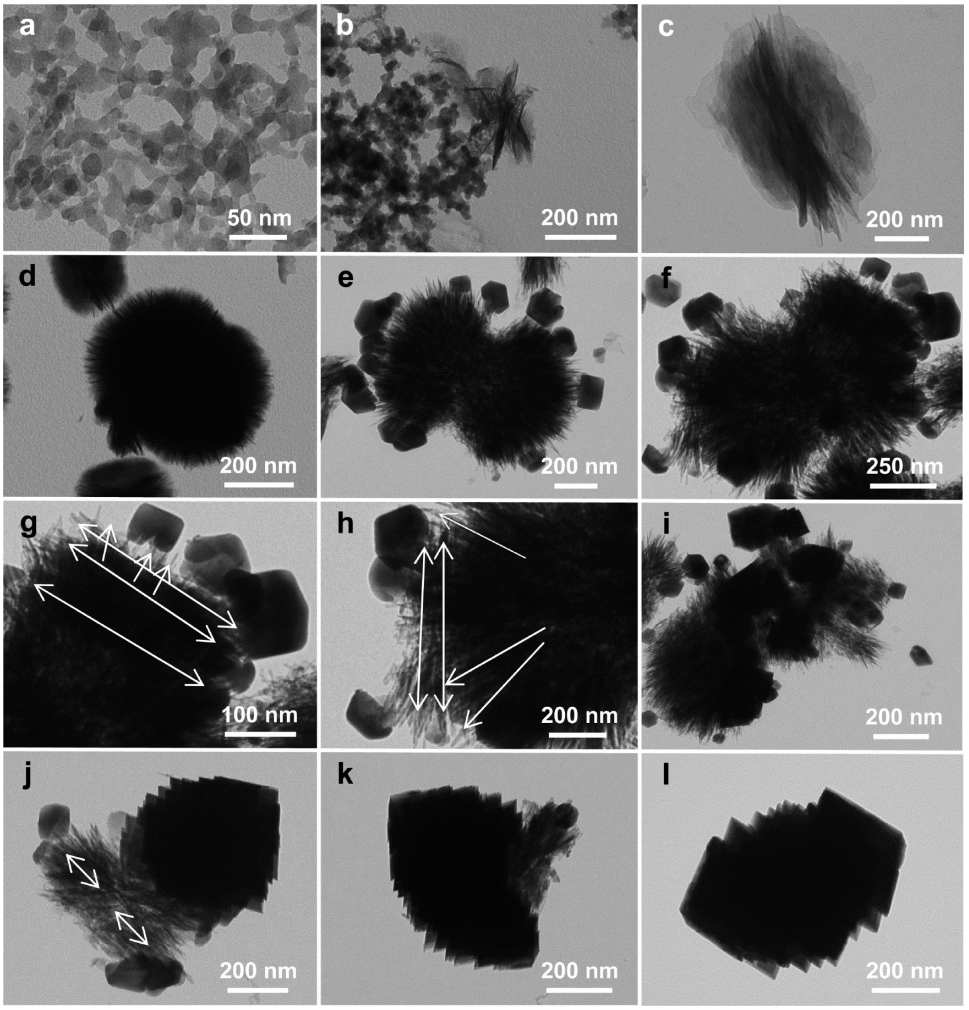

Figure 3. TEM images of the precursors at different stages: (a, b) 82 min; (c) 85 min; (d) 87 min; (e–i) 90 min; (j, k) 95 min; (l) 100 min; and (j) schematic illustration of the growth mechanism for $Zn_{0.33}Co_{0.67}CO_3$ HMBNFs.

To explore the role of n-pentanol in the synthesis of ZnCo-carbonate HMBNFs, we conducted a set of experiments by replacing n-pentanol with other alcohol species while keeping the other parameters unchanged. In the presence of ethanol, mixtures of uneven HMBNFs similar to the typical products and a small amount of spherical hierarchical structures appeared in the final sample (Figure S8a,b). However, as n-pentanol was replaced by polyols such as ethylene glycol or glycerol, the shape of the obtained crystals changed drastically (Figure S8c–f). By comparison, longer straight-chain monoalcohols in the reaction system, i.e. pentanol, could better prompt the formation of micro/nanocrystals assembled by subunits along a specific crystallographic direction than short ones, i.e., ethanol. On the basis of the comparative preliminaries and analyses, the formation of HMBNFs closely pertains to the molecular structure and polarity of n-pentanol. In addition, the experimental results also indicate that the amount of NH_4HCO_3 used in the synthesis is another main factor influencing the shape of the final ZnCo-carbonate sample. As shown in the panoramic FESEM image of Figure S9a, a large quantity of uniform ZnCo-carbonate microspheres was obtained instead of ZnCo-carbonate HMBNFs. Further observation of the high-magnification FESEM images in Figure S9b reveals that numerous quasi-cuboids pile up tightly into microspheres with an average diameter of 3–4 μm. This observation indicates that variation of the amount of NH_4HCO_3 is a useful way to control the size and morphology of the product.

To understand the morphological evolution of the corresponding precursor $Zn_{0.33}Co_{0.67}CO_3$ HMBNFs, we studied the TEM images of the samples in different reaction times, as shown in Figure 3. At the initial stage of the reaction (82 min, Figure 3a,b and 85 min, Figure 3c), numerous flakelike nanoparticle aggregates were obtained; multilayered nanoflake bundles subsequently began to emerge. At 87 min (Figure 3d), hierarchical twin-urchin-spheres formed as more flakes continuously stacked. When the reaction time was prolonged to 90 min (Figure 3e–i), some flakelike nanoparticles started to appear on the 3D hierarchical twin-urchin-spheres. At 95 min, a mixture of twin-urchin-spheres, flakelike nanoparticles and HMBNFs was obtained (Figure 3j, k). Meanwhile, the number of twin-urchin-spheres and flakelike nanoparticles gradually decreased, and these structures subsequently disappeared completely. No obvious change in the morphologies of HMBNFs was observed upon further extension of the reaction time to 100 min or even to 20 h (Figures 3l and 1a–c).

The crystal structure of the product during different time periods was further characterized by XRD presented in the Supporting Information (Figure S10). Curves a–c in Figure

DOI: 10.1021/acsami.5b05303
ACS Appl. Mater. Interfaces 2015, 7, 22848–22857

S10 correspond to reaction times of 82, 85, and 87 min, respectively. No diffraction peak appeared, suggesting that the samples formed were amorphous. When the reaction time was increased to 90 min, weak peaks of ZnCo carbonate were observed, accompanied by the appearance of flakelike nanoparticles. Several of the flake-like particles in the HRTEM images in Figure S11 exhibit uniform lattice fringes with an interplanar distances of 0.20 nm, corresponding very well with the (202) crystal planes of $Zn_{0.33}Co_{0.67}CO_3$, which further confirms that the flakelike particles were crystallized carbonate. The pure and well crystallized phase of ZnCo carbonate was prepared when the reaction time was prolonged to 95 min. The final product with a complete structure of HMBNFs was formed when the reaction time was further extended to 100 min.

Notably, the whole morphological evolution process of the precursor $Zn_{0.33}Co_{0.67}O_3$ occurred within 20 min, which is fast for a crystallization process. Interestingly, the 3D hierarchical twin spheres with an urchinlike structure in Figure 3e did not maintain their morphology, unlike the samples described in previous papers in which the reaction time was prolonged,[22−25] nor did they evolve into 3D twin spheres upon nanoparticle assembly.[26] As shown in Figure 3f, accompanying the crystallization process of ZnCo-carbonate, the transverse nanorods differed in appearance from the longitudinal ones in the two heads of the twin urchinlike spheres; this difference is evident in the magnified images (Figure 3g, h). As shown in Figure 3j, more nanoflakes are formed to construct one multilayered pyramid-like structure and the rest of the region is assembled with transverse nanorods from various angles. Figure 3k shows an almost complete structure of a multilayered bipyramid nanoframe and a small number of transverse nanorods. On the basis of the aforementioned results and analyses, the growth process for $Zn_{0.33}Co_{0.67}CO_3$ HMBNFs is schematically explained in Figure 4. With respect to the generation of architectures, the process usually involves postarrangement of prefabricated building blocks; this postarrangement is induced by numerous driving forces, including capillary effects, surface tension, electric and magnetic forces.[27−36] Here, architectures are constructed from building units formed in situ.[37] In this regard, freshly generated nanofibers cement together side-by-side along the longitudinal direction, undergoing oriented attachment to develop into larger crystals.[38] Simultaneously, nanoflakes self-assemble into framelike hierarchical structures. Notably, in our system, no capping agent was used to protect the nanoflakes. Prompted by the inclination to reduce the surface energy, assembly was apt to occur in face-to-face mode, constricted by the intrinsic geometry.

The electrochemical performance of ZnO/CoO and $ZnCo_2O_4$ HMBNFs was investigated as the anode materials of LIBs. The cyclic voltammetry (CV) curves of ZnO/CoO HMBNFs has been shown in Figure S12a, a sharp peak at 0.56 V in the first cycle leads to the transformation of ZnO/CoO to Co and Zn. The peaks between 0 and 0.4 V are well-known due to the Li−Zn alloying process. Meanwhile, two broad peaks in the range of 0.8−1.1 V and 1.3−1.5 V, different from the one in the first cathodic process, are present in the subsequent processes which could be attributed to structural reorganization, new phase formation, and polarization change in the electrode material.[18,19] Then, two broad oxidation peaks present at 1.6 and 2.0 V and shifted to 1.6 and 2.1 V can be attributed to the phase transformation of Co to CoO and Zn to

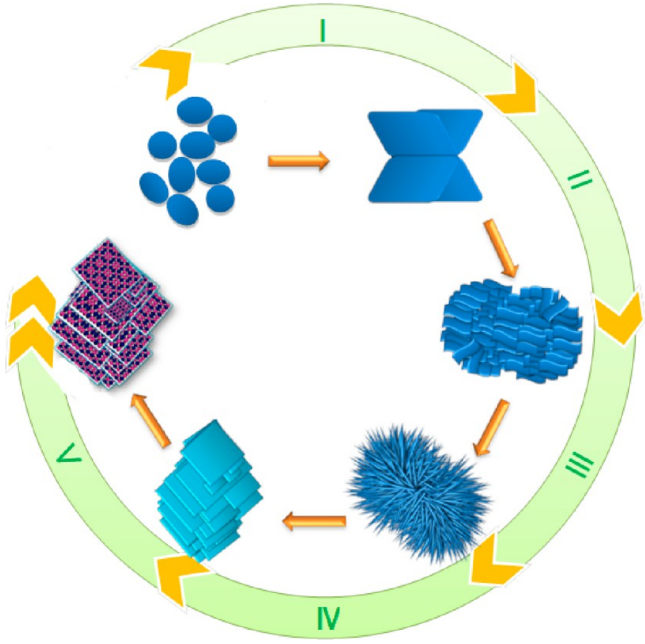

Figure 4. Schematic illustration of the growth mechanism for ZnO/CoO HMBNFs: (I) formation of numerous flakelike nanoparticle aggregates; (II) formation of multilayered nanoflake bundles; (III) formation of 3D hierarchical twin-urchin-spheres; (IV) formation of $Zn_{0.33}Co_{0.67}CO_3$ HMBNFs; (V) formation of ZnO/CoO HMBNFs by thermal decompostion in nitrogen.

ZnO. The CV curves of $ZnCo_2O_4$ HMBNFs have been shown in Figure S12b, wherein, in the first cathodic process, a distinct irreversible peak at about 0.71 V was observed. It could be attributed to the reduction of $ZnCo_2O_4$ to metallic Zn and Co. the peaks between 0 and 0.4 V are ascribed to the Li−Zn alloying process as well. In the first anodic process, there are two broad peaks observed at 1.7 and 2.1 V corresponding to the oxidation reactions of Zn to Zn^{2+} and Co to Co^{2+}. Moreover, the following two anodic processes did not show obvious change in position of the oxidation peaks. By comparison with the first cycle, the reduction peak at about 1.1 V had a prominent voltage shift in the second and third cycles, indicating a different electrochemical mechanism and stability since the second cycle. It should be noted that they indicated similar electrochemical features and there was no great difference in the first three consecutive CVs especially the anodic process. Therefore, according to the results of the CVs in the only first several cycles, it is difficult to ensure the differences for their long cycling performance only by CV, the main reason for the better electrochemical performance could be originating form its bicomponent-active structural feature that could benefit ion diffusion and buffer the volume change during the long electrochemically cycling.

Figure 5a displays the galvanostatic charging and discharging profiles of ZnO/CoO at a current density of 1 A g^{-1}. It delivers a capacity of 1034 mA h g^{-1} during the initial discharge process and a relative low charge capacity of 781.3 mA h g^{-1} with a Coulombic efficiency (CE) of approximately 75.5%. The irreversible capacity loss is likely arised from the formation of a solid electrolyte interphase (SEI), which is observed in anode materials.[39−43] Notably, no obvious changes were observed between the 30th and 50th cycles, indicating that the ZnO/CoO anode exhibits good stability during the cycling process.

DOI: 10.1021/acsami.5b05303
ACS Appl. Mater. Interfaces 2015, 7, 22848−22857

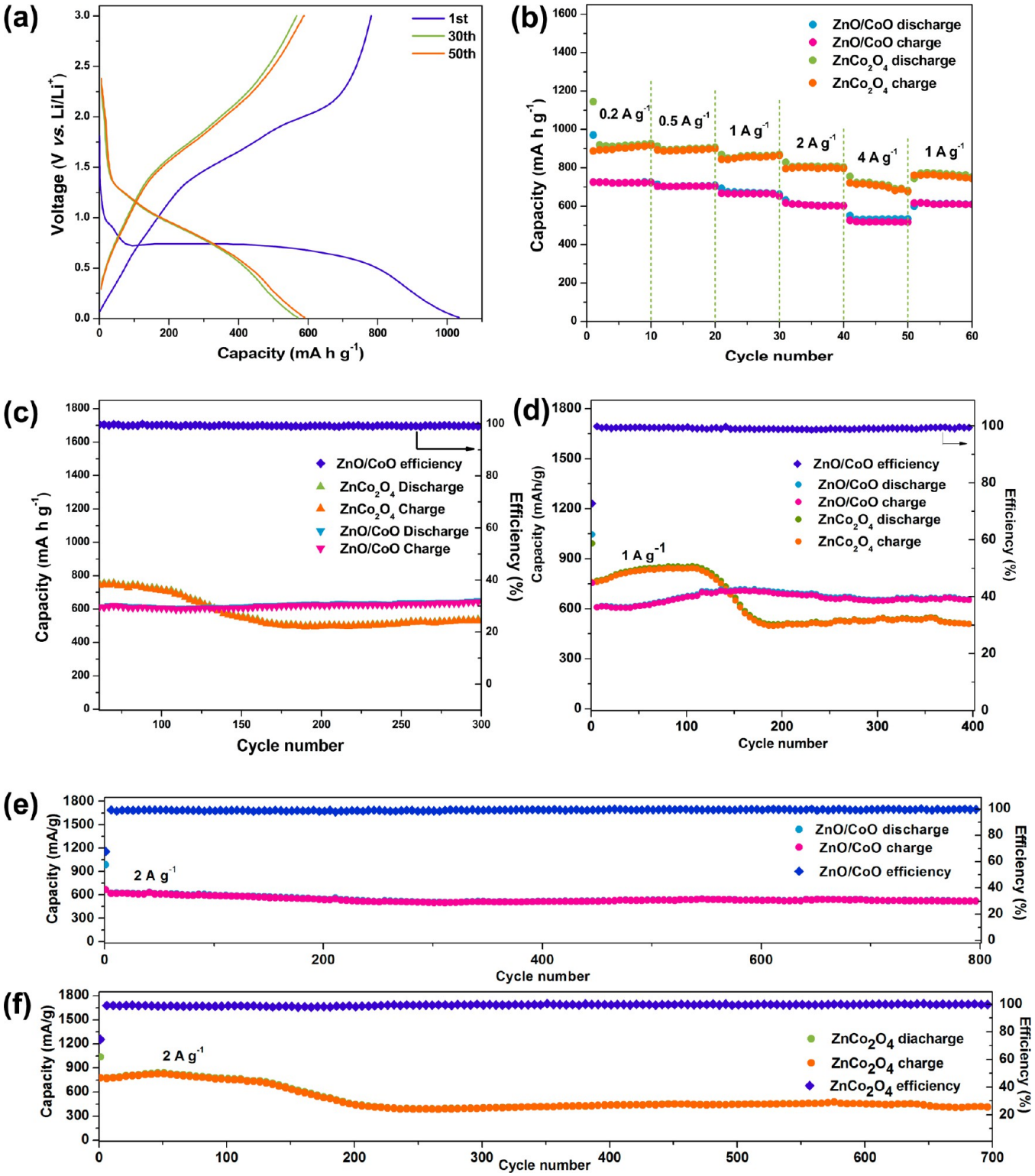

Figure 5. (a) Charge−discharge curves of ZnO/CoO at a current of 1 A g^{-1}. (b) Rate capability of ZnO/CoO. (b) Rate capability of ZnO/CoO at various rates. (c) Cycling performance of ZnO/CoO after the rate test. (d) Cycling performance of ZnO/CoO and $ZnCo_2O_4$ at a current density of 1 A g^{-1}. (e) Cycling performance of ZnO/CoO at a current density of 2 A g^{-1}. (f) Cycling performance of $ZnCo_2O_4$ at a current density of 2 A g^{-1}.

As an important electrochemical characteristic, the rate capability is present in Figure 5b. The reversible capacity of ZnO/CoO was 725, 703.8, 652.7, 602.2, and 517.4 mA h g^{-1}, which was tested at 0.2, 0.5, 1, 2, and 4 A g^{-1}, respectively. When the current density was finally back to 1 A g^{-1}, the reversible capacity was 645 mA h g^{-1} even after 300 cycles, recovering about 98.8% from the first capacity (Figure 5c), suggesting that the ZnO/CoO anode exhibits extremely long cycle life. On the other hand, the rate performance of $ZnCo_2O_4$ was also examined, as shown in Figure 5b. The reversible capacity of $ZnCo_2O_4$ was 915, 895, 860, 800, and 680 mA h g^{-1},which was measured at the current densities of 0.2, 0.5, 1, 2,

DOI: 10.1021/acsami.5b05303
ACS Appl. Mater. Interfaces 2015, 7, 22848−22857

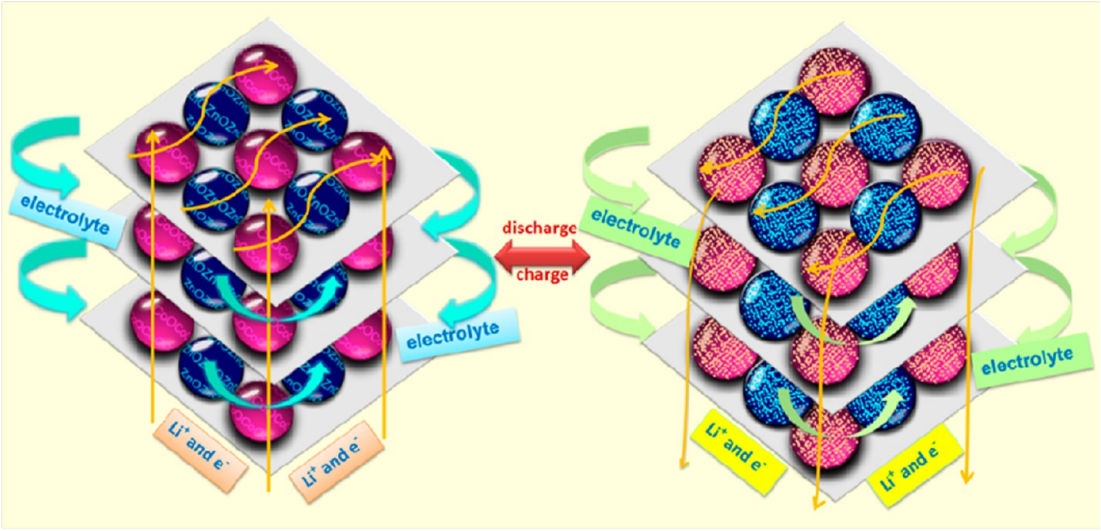

Figure 6. Schematic illustration of the Li^+ insertion−extraction process for ZnO/CoO HMBNFs.

and 4 A g^{-1}, respectively. These results indicate that the performance of the $ZnCo_2O_4$ anode does not substantially differ from that of the ZnO/CoO anode. Notably, however, when the current density was returned to 1 A g^{-1}, a reversible capacity of 540 mA h g^{-1} was measured after 150 cycles, recovering about 62.7% from the first capacity and much lower than that of ZnO/CoO (Figure 5c).

To demonstrate the superior electrochemical performance of ZnO/CoO, we evaluated both the cycling characteristics of ZnO/CoO and $ZnCo_2O_4$ at 1 A g^{-1}. As shown in Figure 5d, the ZnO/CoO composite electrode demonstrates substantially good capacity retention and reversible capacity during cycling. The reversible capacity can still keep approximately 664 mA h g^{-1} even after 400 cycles, with no losses compared to the second cycle (612 mA h g^{-1} at the second cycle). Furthermore, the CE of the ZnO/CoO composite electrode rapidly increases from ~66% for the first cycle to approximately 99% after two cycles and maintains nearly 100% thereafter. This result indicates a convenient Li^+ insertion/extraction process associated with the efficient transport of ions and electrons in the electrodes. As for $ZnCo_2O_4$ HMBNFs, the capacity decreases very rapidly during the course of 100 cycles and only approximately 66% of the second-cycle discharge capacity is retained. To further confirm the excellent durability and the advantages of the ZnO/CoO and $ZnCo_2O_4$ HMBNFs, we tested the long-term cycling performance of both samples at a current density of 2 A g^{-1}, as shown in Figure 5e and f, respectively. The reversible capacity of ZnO/CoO is 518 mA h g^{-1} after 800 cycles, with a retention rate of approximately 83% of the second-cycle discharge capacity. According to this, the capacity fading rate is approximately 0.13 mA h g^{-1} per cycle after the second cycle. The result is better than the reported ZnO−CoO−C nanowall arrays[44] and CoO-involved anodes.[8] In addition, the reversible capacity of $ZnCo_2O_4$ is only 409 mA h g^{-1} after 700 cycles, with a retention rate of only 53% and the capacity fading rate greater than 0.52 mA h g^{-1} per cycle after the second cycle. By comparison with other reports about $ZnCo_2O_4$ as anode materials of LIBs,[45,46] the prepared $ZnCo_2O_4$ HMBNFs offer satisfying lithium-ion storage performance.

The superior electrochemical performance of ZnO/CoO HMBNFs is attributable to its unique homogeneous nano-hybrid hierarchical architecture, as illustrated in Figure 6. First, the ZnO/CoO HMBNFs' multilayered structure composed of nanosized subunits can provide more contact positions for the electrolyte and Li^+, and their mesoporous structure can not only facilitate the fast diffusion of Li^+ but also alleviate the volume change during the Li^+ insertion/extraction process. Second, and more importantly, the ZnO/CoO HMBNFs are homogeneous 3D nanohybrids in which ZnO and CoO occupy their own nanoscale regions; hence the enhanced electrochemical activity of these HMBNFs is closely related to the possible synergetic effects between the bicomponent activity of ZnO and CoO. Third, ZnO nanoparticles, which are well-dispersed in the hybrid, apparently serve as buffer domains to spatially separate the coexisting CoO phase. Hence, the aggregation of CoO can be efficiently prevented during repeated Li^+ insertion/extraction, thereby facilitating the capacity retention of the ZnO/CoO HMBNF electrode. Furthermore, because of their nanoscale dimensions, the composite ZnO/CoO HMBNFs consist of uniform crystal domains of CoO and ZnO nanocrystals, also alleviating the strain resulting from volume variation during cycles. As a result, the ZnO/CoO nanohybrids exhibit excellent long-term cycling performance with good cycle stability and a low capacity fading rate.

4. CONCLUSIONS

In summary, we first demonstrated a facile method for the shape-controlled synthesis of novel ordered ZnO/CoO and $ZnCo_2O_4$ HMBNFs. Flakelike nanoparticle aggregates and multilayered nanoflakes form during the early stage of the reaction, followed by growth of 3D hierarchical twin-urchin spheres and flakelike nanoparticles as well as the final formation of the HMBNF structures. The introduction of different amounts of NH_4HCO_3 into the system allows for the shape-controlled synthesis of HMBNFs. The use of an appropriate straight-chain monoalcohol was observed to be critical for the formation of HMBNFs. An extremely fast crystal growth process and an unusual transverse crystallization of the ZnCo-carbonate HMBNFs were newly discovered and proposed. The ZnO/CoO HMBNFs feature high rate performance, and especially long cycle stability. It is concluded that the superior electrochemical performance of this material is attributable to

DOI: 10.1021/acsami.5b05303
ACS Appl. Mater. Interfaces 2015, 7, 22848−22857

its unique nanostructure, its bicomponent active synergy, the uniform distribution of ZnO and CoO phases at the nanoscale level, and the Li alloying reaction. Given the facile synthetic method that forms the unique nanostructure by an unusual transverse crystallization, the ZnO/CoO HMBNF has the prospect of becoming an excellent anode material for next-generation LIBs. This work provides a versatile approach to the synthesis of ordered heterohierarchical nanoframes.

■ ASSOCIATED CONTENT

Supporting Information

The Supporting Information is available free of charge on the ACS Publications website at DOI: 10.1021/acsami.5b05303.

XRD patterns, FESEM images, HRTEM, and TGA data of the precursor, XPS spectra, nitrogen physisorption isotherms and pore size distribution curves, EDX, and CV curves of ZnO/CoO and $ZnCo_2O_4$ HMBNFs (PDF)

■ AUTHOR INFORMATION

Corresponding Author

*E-mail: chexsl@sdu.edu.cn.

Notes

The authors declare no competing financial interest.

■ ACKNOWLEDGMENTS

This study was supported by the National Basic Research Program of China (grant 2011CB935901), Shandong Provincial Natural Science Foundation for Distinguished Young Scholar (grant JQ201304), National Natural Science Fund of China (grants 21371108 and 21203110), and Zhejiang Normal University, Jinhua 321004, China (Grant ZJHX201505).

■ REFERENCES

(1) Dunn, B.; Kamath, H.; Tarascon, J.-M. Electrical Energy Storage for the Grid: A Battery of Choices. *Science* **2011**, *334*, 928−935.

(2) Bruce, P. G.; Scrosati, B.; Tarascon, J.-M. Nanomaterials for Rechargeable Lithium Batteries. *Angew. Chem., Int. Ed.* **2008**, *47*, 2930−2946.

(3) Ji, X.; Lee, K. T.; Nazar, L. F. A Highly Ordered Nanostructured Carbon−Sulphur Cathode for Lithium−Sulphur Batteries. *Nat. Mater.* **2009**, *8*, 500−506.

(4) Choi, N. S.; Chen, Z.; Freunberger, S. A.; Ji, X. Y.; Sun, K.; Yushin, K. G.; Nazar, L. F.; Cho, J.; Bruce, P. G. Challenges Facing Lithium Batteries and Electrical Double-Layer Capacitors. *Angew. Chem., Int. Ed.* **2012**, *51*, 9994−10024.

(5) Lou, X. W.; Archer, L. A.; Yang, Z. Hollow Micro-/Nanostructures: Synthesis and Applications. *Adv. Mater.* **2008**, *20*, 3987−4019.

(6) Hong, Y. J.; Son, M. Y.; Kang, Y. C. One-Pot Facile Synthesis of Double-Shelled SnO_2 Yolk-Shell-Structured Powders by Continuous Process as Anode Materials for Li-ion Batteries. *Adv. Mater.* **2013**, *25*, 2279−2283.

(7) Li, H.; Wang, Z. X.; Chen, L. Q.; Huang, X. J. Research on Advanced Materials for Li-ion Batteries. *Adv. Mater.* **2009**, *21*, 4593−4607.

(8) Xiong, S. L.; Chen, J. S.; Lou, X. W.; Zeng, H. C. Mesoporous Co_3O_4 and CoO@C Topotactically Transformed from Chrysanthemum-like $Co(CO_3)_{0.5}(OH)\cdot 0.11H_2O$ and Their Lithium-Storage Properties. *Adv. Funct. Mater.* **2012**, *22*, 861−871.

(9) Wang, Y.; Zhang, H. J.; Lu, L.; Stubbs, L. P.; Wong, C. C.; Lin, J. Y. Designed Functional Systems from Peapod-like Co@Carbon to Co_3O_4@Carbon Nanocomposites. *ACS Nano* **2010**, *4*, 4753−4761.

(10) Thapa, A. K.; Pandit, B.; Thapa, R.; Luitel, T.; Paudel, H. S.; Sumanasekera, G.; Sunkara, M.; Gunawardhana, N.; Ishihara, T.; Yoshio, M. Synthesis of Mesoporous Birnessite-MnO_2 Composite as a Cathode Electrode for Lithium Battery. *Electrochim. Acta* **2014**, *116*, 188−193.

(11) Han, F.; Li, D.; Li, W. C.; Lei, C.; Sun, Q.; Lu, A. H. Nanoengineered Polypyrrole-Coated Fe_2O_3@C Multifunctional Composites with an Improved Cycle Stability as Lithium-Ion Anode. *Adv. Funct. Mater.* **2013**, *23*, 1692−1700.

(12) Sun, Y. M.; Hu, X. L.; Luo, W.; Huang, Y. H. Self-Assembled Hierarchical MoO_2/Graphene Nanoarchitectures and Their Application as a High-Performance Anode Material for Lithium-Ion Batteries. *ACS Nano* **2011**, *5*, 7100−7107.

(13) Huang, X. L.; Wang, R. Z.; Xu, D.; Wang, Z. L.; Wang, H. G.; Xu, J. J.; Wu, Z.; Liu, Q. C.; Zhang, Y.; Zhang, X. B. Homogeneous CoO on Graphene for Binder-Free and Ultralong-Life Lithium Ion Batteries. *Adv. Funct. Mater.* **2013**, *23*, 4345−435.

(14) He, C.; Wu, S.; Zhao, N. Q.; Shi, C. S.; Liu, E. Z.; Li, J. J. Mesoporous Fe_3O_4@C Submicrospheres Evolved from a Novel Self-corrosion Mechanism for High-Performance Lithium-Ion Batteries. *ACS Nano* **2013**, *7*, 4459−4469.

(15) Zhou, X. S.; Dai, Z. H.; Liu, S. H.; Bao, J. C.; Guo, Y. G. Ultra-Uniform SnO_x/Carbon Nanohybrids toward Advanced Lithium-Ion Battery Anodes. *Adv. Mater.* **2014**, *26*, 3943−3949.

(16) Zhang, H. W.; Zhou, L.; Noonan, O.; Martin, D. J.; Whittaker, A. K.; Yu, C. Z. Tailoring the Void Size of Iron Oxide@Carbon Yolk−Shell Structure for Optimized Lithium Storage. *Adv. Funct. Mater.* **2014**, *24*, 4337−4342.

(17) Li, X. W.; Xiong, S. L.; Li, J. F.; Liang, X.; Wang, J. Z.; Bai, J.; Qian, Y. T. Constructed Functional Systems from Mn_2O_3 Nanowires to MnO@Carbon Core-Shell Nanowires as Stable High-Performance Anodes for Lithium-Ion Batteries. *Chem. - Eur. J.* **2013**, *19*, 11310−11319.

(18) Li, M. X.; Yin, Y. X.; Li, C. J.; Zhang, F. Z.; Wan, L. J.; Xu, S. L.; Evans, D. G. Well-Dispersed Bi-Component-active CoO/$CoFe_2O_4$ Nanocomposites with Tunable Performances as Anode Materials for Lithium-Ion Batteries. *Chem. Commun.* **2012**, *48*, 410−412.

(19) Hou, L. R.; Lian, L.; Zhang, L. H.; Pang, G.; Yuan, C. Z.; Zhang, X. G. Self-Sacrifice Template Fabrication of Hierarchical Mesoporous Bi-Component-Active ZnO/$ZnFe_2O_4$ Sub-Microcubes as Superior Anode Towards High-Performance Lithium-Ion Battery. *Adv. Funct. Mater.* **2015**, *25*, 238−246.

(20) Rai, A. K.; Gim, J.; Thi, T. V.; Ahn, D.; Cho, S. J.; Kim, J. High Rate Capability and Long Cycle Stability of Co_3O_4/$CoFe_2O_4$ Nanocomposite as an Anode Material for High-Performance Secondary Lithium Ion Batteries. *J. Phys. Chem. C* **2014**, *118*, 11234−11243.

(21) Sharma, Y.; Sharma, N.; Rao, G. V. S.; Chowdari, B. V. R. Nanophase $ZnCo_2O_4$ as a High Performance Anode Material for Li-Ion Batteries. *Adv. Funct. Mater.* **2007**, *17*, 2855−2861.

(22) Xiao, Y. H.; Liu, S. J.; Li, F.; Zhang, A. Q.; Zhao, J. H.; Fang, S. M.; Jia, D. Z. 3D Hierarchical Co_3O_4 Twin-Spheres with an Urchin-Like Structure: Large-Scale Synthesis, Multistep-Splitting Growth, and Electrochemical Pseudocapacitors. *Adv. Funct. Mater.* **2012**, *22*, 4052−4059.

(23) Tang, J.; Alivisatos, A. P. Crystal Splitting in the Growth of Bi_2S_3. *Nano Lett.* **2006**, *6*, 2701−2706.

(24) Shen, X. F.; Yan, X. P. Facile Shape-Controlled Synthesis of Well-Aligned Nanowire Architectures in Binary Aqueous Solution. *Angew. Chem., Int. Ed.* **2007**, *46*, 7659−7663.

(25) Li, L.; Sun, N.; Huang, Y.; Qin, Y.; Zhao, L. S.; Gao, J.; Li, M.; Zhou, H.; Qi, L. Topotactic Transformation of Single-Crystalline Precursor Discs into Disc-Like Bi_2S_3 Nanorod Networks. *Adv. Funct. Mater.* **2008**, *18*, 1194−1201.

(26) Bai, J.; Li, X. G.; Liu, G. Z.; Qian, Y. T.; Xiong, S. L. Unusual Formation of $ZnCo_2O_4$ 3D Hierarchical Twin Microspheres as a High-Rate and Ultralong-Life Lithium-Ion Battery Anode Material. *Adv. Funct. Mater.* **2014**, *24*, 3012−3020.

(27) Bowden, N.; Terfort, A.; Carbeck, J.; Whitesides, G. M. Self-Assembly of Mesoscale Objects into Ordered Two-Dimensional Arrays. *Science* **1997**, *276*, 233−235.

DOI: 10.1021/acsami.5b05303
ACS Appl. Mater. Interfaces 2015, 7, 22848−22857

(28) Gracias, D. H.; Tien, J.; Breen, T. L.; Hsu, C.; Whitesides, G. M. Forming Electrical Networks in Three Dimensions by Self-Assembly. *Science* **2000**, *289*, 1170−1172.
(29) Whitesides, G. M.; Grzybowski, B. Self-Assembly at All Scales. *Science* **2002**, *295*, 2418−2421.
(30) Thalladi, V. R.; Whitesides, G. M. Crystals of Crystals: Fabrication of Encapsulated and Ordered Two-Dimensional Arrays of Microcrystals. *J. Am. Chem. Soc.* **2002**, *124*, 3520−3521.
(31) Wu, H.; Thalladi, V. R.; Whitesides, S.; Whitesides, G. M. Using Hierarchical Self-Assembly to Form Three-Dimensional Lattices of Spheres. *J. Am. Chem. Soc.* **2002**, *124*, 14495−14502.
(32) Love, J. C.; Urbach, A. R.; Prentiss, M. G.; Whitesides, G. M. Three-Dimensional Self-Assembly of Metallic Rods with Submicron Diameters Using Magnetic Interactions. *J. Am. Chem. Soc.* **2003**, *125*, 12696−12697.
(33) Colfen, H.; Mann, S. Higher-Order Organization by Mesoscale Self-Assembly and Transformation of Hybrid Nanostructures. *Angew. Chem., Int. Ed.* **2003**, *42*, 2350−2365.
(34) Velikov, K. P.; Christova, C. G.; Dullens, R. P. A.; Blaaderen, A. Layer-by-Layer Growth of Binary Colloidal Crystals. *Science* **2002**, *296*, 106−109.
(35) Kim, F.; Kwan, S.; Akana, J.; Yang, P. Langmuir-Blodgett Nanorod Assembly. *J. Am. Chem. Soc.* **2001**, *123*, 4360−4361.
(36) Dinsmore, A. D.; Hsu, M. F.; Nikolaides, M. G.; Marquez, M.; Bausch, A. R.; Weitz, D. A. Colloidosomes: Selectively Permeable Capsules Composed of Colloidal Particles. *Science* **2002**, *298*, 1006−1009.
(37) Liu, B.; Zeng, H. C. Fabrication of ZnO "Dandelions" via a Modified Kirkendall Process. *J. Am. Chem. Soc.* **2004**, *126*, 8124−8125.
(38) Kolthoff, I. M.; Noponen, G. E. Studies on Aging of Fresh Precipitates. XIX. Aging of Freshly Precipitated Barium Sulfate in Dilute Barium and Sulfate Solutions. *J. Am. Chem. Soc.* **1938**, *60*, 499−505.
(39) Demir-Cakan, R.; Hu, Y.-S.; Antonietti, M.; Maier, J.; Titirici, M.-M. Facile One-Pot Synthesis of Mesoporous SnO_2 Microspheres via Nanoparticles Assembly and Lithium Storage Properties. *Chem. Mater.* **2008**, *20*, 1227−1229.
(40) Wang, H.; Cui, L.-F.; Yang, Y.; Sanchez Casalongue, H.; Robinson, J. T.; Liang, Y.; Cui, Y.; Dai, H. Mn_3O_4−Graphene Hybrid as a High-Capacity Anode Material for Lithium Ion Batteries. *J. Am. Chem. Soc.* **2010**, *132*, 13978−13980.
(41) Lee, S. W.; Yabuuchi, N.; Gallant, B. M.; Chen, S.; Kim, B.-S.; Hammond, P. T.; Shao-Horn, Y. High-Power Lithium Batteries from Functionalized Carbon-Nanotube Electrodes. *Nat. Nanotechnol.* **2010**, *5*, 531−537.
(42) Laruelle, S.; Grugeon, S.; Poizot, P.; Dolle, M.; Dupont, L.; Tarascon, J. M. On the Origin of the Extra Electrochemical Capacity Displayed by MO/Li Cells at Low Potential. *J. Electrochem. Soc.* **2002**, *149*, A627−A634.
(43) Yang, S. B.; Feng, X. L.; Ivanovici, S.; Mullen, K. Fabrication of Graphene-Encapsulated Oxide Nanoparticles: Towards High-Performance Anode Materials for Lithium Storage. *Angew. Chem., Int. Ed.* **2010**, *49*, 8408−8441.
(44) Wu, Z.; Qin, L.; Pan, Q. Fabrication and electrochemical behavior of flower-like ZnO−CoO−C nanowall arrays as anodes for lithium-ion batteries. *J. Alloys Compd.* **2011**, *509*, 9207−9213.
(45) Giri, A. K.; Pal, P.; Ananthakumar, R.; Jayachandran, M.; Mahanty, S.; Panda, A. B. 3D Hierarchically Assembled Porous Wrinkled-Paper-like Structure of $ZnCo_2O_4$ and Co-ZnO@C as Anode Materials for Lithium-Ion Batteries. *Cryst. Growth Des.* **2014**, *14*, 3352−3359.
(46) Sharma, Y.; Sharma, N.; Subba Rao, G. V.; Chowdari, B. V. R. Nanophase $ZnCo_2O_4$ as a High Performance Anode Material for Li-Ion Batteries. *Adv. Funct. Mater.* **2007**, *17*, 2855−2861.

DOI: 10.1021/acsami.5b05303
ACS Appl. Mater. Interfaces 2015, 7, 22848−22857